Theoretical and numerical simulation of bulk and surface ultrasonic waves scattering in microstructures with elongated grains

Juan Camilo Victoria Giraldo, Bing Tie

CSMA 2024
16ème Colloque National en Calcul des Structures
13-17 Mai 2024, Presqu'île de Giens (Var)

Theoretical and numerical modeling of bulk and surface ultrasonic waves scattering in polycrystalline microstructures with elongated grains

Juan Camilo Victoria Giraldo[1], Bing Tie[1]

[1] *Université Paris-Saclay, CentraleSupélec, ENS Paris-Saclay, CNRS, LMPS, {juan-camilo.victoria-giraldo,bing.tie}@centralesupelec.fr*

Abstract — In the present work, the grain scattering induced attenuation coefficient is obtained for longitudinal bulk waves in untextured cubic polycrystalline materials with elongated grains using theoretical 2D and 3D proposed models. Also, a semi-analytical approach to estimate the attenuation of Rayleigh waves is used. Numerical simulations are done with a finite element code using a space-discontinuous Galerkin method and a Runge-Kutta time discretization scheme. The numerical and theoretical results are compared to study the influence of the grain shape/rotation on the attenuation coefficient.
Mots clés — Space-discontinuous Galerkin method, ultrasonic attenuation, polycrystalline materials.

1 Introduction

Ultrasonic scattering can be studied by looking closer at ultrasonic amplitude attenuation and wave phase velocity. In polycrystalline materials, scattering is mainly a result of wave interaction with the material inhomogeneities. Indeed, in polycrystalline materials, the inhomogeneities can be summarized in the relative crystallographic misorientation from grain to grain and the possible presence of multiple phases. When it comes to surface waves, the unevenness of the boundary becomes also of interest. In particular, knowledge about the influence and relation of these inhomogeneities (grain size and shape, degree of anisotropy, surface roughness, etc.) in ultrasonic attenuation is essential, as useful microstructural information can be applied to characterization and defect control methodologies.

Several theoretical models have been developed, with earlier models devoting attention to the case of randomly oriented, cubic crystals and equiaxed grains with the introduction of a two-point correlation (TPC) spatial isotropic function. Stanke and Kino [1] introduced a unified theory that accounts for an order of multiple scattering, based on Karal and Keller's [2] approximation. Weaver [3], on the contrary, based his work on Dyson's equation. These two models also have led to extensions considering more general grain shapes. Ahmed *et al.* [4] followed the work of Stanke and Kino [1] by introducing a transverse isotropic TPC function. Yang *et al.* [5], implemented a general anisotropic function in Weaver's [3] equations and obtained a closed-form expression. Also, Calvet and Margerin [6] proposed a spectral approach based on the work of Weaver [3] and Yang *et al.* [5], obtaining results up to the geometric frequency region. Numerical simulations have been also carried out in equiaxed grains [7] and elongated grains [8].

Regarding the study of surface wave scattering due to grain boundaries, Kaganova and Maradudin [9] were able to obtain the dispersion relation for Rayleigh waves propagating in the plane surface of a polycrystalline medium. More recently, Ryzy *et al.* [10] compared experimental Rayleigh wave attenuation values with a proposed semi-analytical attenuation model, obtaining a somewhat good agreement in the stochastic scattering region.

Few works have dealt with 2D ultrasonic scattering, which remains an interesting problem insofar as it makes it possible to compare 2D and 3D models, analyze the dimensionality of grain diffusion phenomena, and better understand their mechanism. In this work, Bai and Tie's model [11, 12] for bulk waves is recalled and then extended to the general case of elongated grains of ellipsoidal shape for the 2D and 3D cases. Also, the methodology proposed by Ryzy *et al.* [10] is used to investigate in a first approach the attenuation of Rayleigh waves in microstructures with elongated grains. Our theoretical model is compared with numerical results, with emphasis on the main differences and similarities between 3D and 2D results.

2 General theoretical ultrasonic attenuation framework

2.1 Bulk waves ultrasonic attenuation considering elongated grains

This work follows the theoretical studies after Stanke and Kino's [1] unified theory. The objective here is to recall the equations used as a framework and extend Bai and Tie's [11, 12] model to the case of elongated grains.

Considering an ensemble of possible inhomogeneous media made of the same single polycrystalline material and occupying $\Omega \subset \mathbf{R}^{dim}, dim = 2,3$. The polycrystalline material is defined by a position-dependent elastic tensor $\boldsymbol{C}(\boldsymbol{x})$ and a constant density ρ. Following the proposed second-order series on ε, the anisotropy factor, from [2], for the average expected propagating wave $\langle \boldsymbol{u} \rangle$, the following equation for $\langle \boldsymbol{u} \rangle$ can be obtained:

$$\boldsymbol{L}\langle \boldsymbol{u} \rangle - \varepsilon \langle \boldsymbol{L}_1 \rangle \langle \boldsymbol{u} \rangle - \varepsilon^2 \left[\langle \boldsymbol{L}_1 \boldsymbol{L}^{-1} \boldsymbol{L}_1 \rangle - \langle \boldsymbol{L}_1 \rangle \boldsymbol{L}^{-1} \langle \boldsymbol{L}_1 \rangle + \langle \boldsymbol{L}_2 \rangle \right] \langle \boldsymbol{u} \rangle = 0 \tag{1}$$

In our case, the perturbation operators $\boldsymbol{L}$ and $\boldsymbol{L}_1$ can be defined as:

$$\boldsymbol{L} = \rho\omega^2 \boldsymbol{u}(\boldsymbol{x}) + \nabla_x \left(\boldsymbol{C}^0 : \varepsilon(\boldsymbol{u}(\boldsymbol{x})) \right), \quad \varepsilon^2 \boldsymbol{L}_1 = \nabla_x \left(\delta \boldsymbol{C}(\boldsymbol{x}) : \varepsilon(\boldsymbol{u}(\boldsymbol{x})) \right), \quad \varepsilon^n \boldsymbol{L}_n = 0, \forall n > 1 \tag{2}$$

The deviation of the elastic tensor is considered to be the deviation of the heterogeneous medium from its equivalent homogeneous medium $\delta \boldsymbol{C}(\boldsymbol{x}) = \boldsymbol{C}(\boldsymbol{x}) - \boldsymbol{C}^0$. The elastic tensor $\boldsymbol{C}^0$ is an equivalent homogeneous tensor chosen as the Voigt average. This allows to define the operator $\boldsymbol{L}^{-1}$ as:

$$\boldsymbol{L}^{-1} \boldsymbol{u}(\boldsymbol{x}) = \int \boldsymbol{G}^T(\boldsymbol{x}'; \boldsymbol{x}) \boldsymbol{u}(\boldsymbol{x}') d\boldsymbol{x}' \tag{3}$$

where $\boldsymbol{G}(\boldsymbol{x}'; \boldsymbol{x})$ is the dyadic Green function tensor. Furthermore, we consider the assumptions of single-phase material and randomly oriented crystallographic axes, which means on average the medium is isotropic $\langle \delta \boldsymbol{C}(\boldsymbol{x}) \rangle = 0$. Also, assuming that the elastic tensor varies independently from grain to grain, the following simplification for the elastic autocorrelation function can be made $\langle \delta \boldsymbol{C}(\boldsymbol{x}) \otimes \delta \boldsymbol{C}(\boldsymbol{x}') \rangle = \langle \delta \boldsymbol{C}^g \otimes \delta \boldsymbol{C}^g \rangle W(\boldsymbol{r})$. Where $\delta \boldsymbol{C}^g$ is the elastic tensor variation in each grain which is constant. The average is considered to be the average overall crystallographic orientations, and the two-point correlation (TPC) spatial function $W(\boldsymbol{r})$ is the function responsible for the characteristic grain geometry description by estimating the probability of two random points $\boldsymbol{x}$ and $\boldsymbol{x}'$ being in the same grain, with $\boldsymbol{r} = \boldsymbol{x} - \boldsymbol{x}'$.

Bai *et al.'s* [12] final expressions are obtained after applying the Born approximation, and therefore, the here presented results are only valid in the Rayleigh and stochastic scattering regions. Then, solving for the complex-valued wavenumber k, the following expressions for the attenuation can be obtained:

$$\alpha^{\beta\gamma,2D} = \mathrm{Im}\left(\frac{k_{0\beta} \langle \delta C_{j^\beta jkl} \delta C_{mnj^\beta j} \rangle}{2C^0_{j^\beta j j^\beta j}} \int_{r=0}^{\infty} \int_{\theta=0}^{2\pi} G^\gamma_{km}(r,\theta) D^\beta_{ln}(r,\theta) r d\theta dr \right) \quad \beta,\gamma = L,T \tag{4a}$$

$$\alpha^{\beta\gamma,3D} = \mathrm{Im}\left(\frac{k_{0\beta} \langle \delta C_{j^\beta jkl} \delta C_{mnj^\beta j} \rangle}{2C^0_{j^\beta j j^\beta j}} \int_{r=0}^{\infty} \int_{\theta=0}^{\pi} \int_{\varphi=0}^{2\pi} G^\gamma_{km}(r,\theta,\varphi) D^\beta_{ln}(r,\theta,\varphi) r^2 \sin\theta d\varphi d\theta dr \right) \tag{4b}$$

where G^γ_{km} is the dyadic Green function in a 2D or 3D isotropic homogeneous medium, and its expression can be found in equations (16, 17) in [12] and $D^\beta_{ln} = \frac{\partial^2 W(\boldsymbol{r}) e^{ik\hat{\boldsymbol{k}}\cdot\boldsymbol{r}}}{\partial r_n \partial r_l}$ is a second order derivative tensor.

In the 3D case, one can assume the elongated grains to have an ellipsoidal geometric shape. The assumed grain shape can be represented by the anisotropic TPC function (5), which is the extended form of the equiaxed TPC function. This function has been already used by [4], [5] and [6].

$$W(\boldsymbol{r}) = e^{-\sqrt{\boldsymbol{r}^T \boldsymbol{A} \boldsymbol{r}}}, \boldsymbol{A} = \sum_{i=1}^{3} \frac{1}{a_i^2} \boldsymbol{g}_i \otimes \boldsymbol{g}_i \tag{5}$$

In equation (5), $\boldsymbol{A}$ is a second-order symmetric tensor composed by the inverse of a_1^2, a_2^2, a_3^2, the ellipsoidal radii in the local coordinate system of the ellipsoid $(\boldsymbol{g}_1, \boldsymbol{g}_2, \boldsymbol{g}_3)$. In the definition of $\boldsymbol{A}$, the rotation of the grain is implicit, with its basis depending on the angles τ and φ_τ. These angles define the orientation of the axis $\boldsymbol{g}_3$ as shown in Figure 1.

The function (5) leads to:

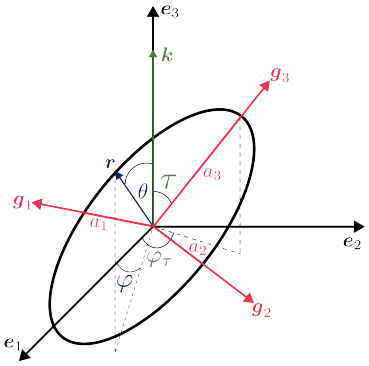

Figure 1: Illustration of an ellipsoidal grain, where a_1, a_2, a_3 are the ellipsoidal radii and τ, φ_τ are the orientation angles of the ellipsoid principal axis $\boldsymbol{g}_3$ and θ, φ are the angles of the vector $\boldsymbol{r}$.

$$\boldsymbol{D}^{\beta}(\boldsymbol{r}) = \left[-\frac{\boldsymbol{A}}{r} + \left(\frac{1}{r(\hat{\boldsymbol{r}}^T \boldsymbol{A}\hat{\boldsymbol{r}})} + \frac{1}{\sqrt{\hat{\boldsymbol{r}}^T \boldsymbol{A}\hat{\boldsymbol{r}}}} \right) (\boldsymbol{A}\hat{\boldsymbol{r}}) \otimes (\boldsymbol{A}\hat{\boldsymbol{r}}) - 2ik_{0\beta}\hat{\boldsymbol{k}} \otimes_s (\boldsymbol{A}\hat{\boldsymbol{r}}) - \sqrt{\hat{\boldsymbol{r}}^T \boldsymbol{A}\hat{\boldsymbol{r}}} k_{0\beta}^2 \hat{\boldsymbol{k}} \otimes \hat{\boldsymbol{k}} \right] \times \frac{e^{r\left(ik_{0\beta}\hat{\boldsymbol{k}}\cdot\hat{\boldsymbol{r}} - \sqrt{\hat{\boldsymbol{r}}^T \boldsymbol{A}\hat{\boldsymbol{r}}}\right)}}{\sqrt{\hat{\boldsymbol{r}}^T \boldsymbol{A}\hat{\boldsymbol{r}}}} \tag{6}$$

where $r = \|\boldsymbol{r}\|$. We can define $R = a_3/a_1$ and $R_1 = a_2/a_1$ as the two aspect ratios of the ellipsoid. The grain can take any possible configuration in each axis of elongation $\boldsymbol{g}_3$ and $\boldsymbol{g}_2$ by tunning the ratios R and R_1 (cigar or pancake shape).

In the 2D case, one can start with an elongated 3D ellipsoidal grain and analyze a 2D cutting plane section defined by a unit vector $\hat{\boldsymbol{n}}$. A 2D plane in a 3D microstructure might cut the grains into multiple cross-sections. Here, we simplify by assuming that the 2D plane cuts the grains always by its center. The intersection of an ellipsoid and a cutting plane will always result in an ellipse or a sphere at least.

One can define a plane $\boldsymbol{t}_1, \boldsymbol{t}_2$ perpendicular to the defined normal unit vector $\hat{\boldsymbol{n}}$. As we decided to fix $\hat{\boldsymbol{k}} = \boldsymbol{e}_3$, we can set the axis $\boldsymbol{t}_2 = \hat{\boldsymbol{k}}$, and find $\boldsymbol{t}_1 = \hat{\boldsymbol{k}} \times \hat{\boldsymbol{n}}$. It can be found that $\boldsymbol{A}^{2D}$ can be written in terms of $\boldsymbol{A}^{3D}, \boldsymbol{t}_1, \boldsymbol{t}_2$ as:

$$\boldsymbol{A}^{2D} = \sum_{i,j=1}^{2} (\boldsymbol{t}_j \boldsymbol{A}^{3D} \boldsymbol{t}_i) \boldsymbol{t}_i \otimes \boldsymbol{t}_j \tag{7}$$

Here, $\boldsymbol{A}^{2D}$ as in the 3D case, is a second-order symmetric tensor. It describes an ellipse in the orthonormal pair $\boldsymbol{t}_1, \boldsymbol{t}_2$. Since we decided to fix $\boldsymbol{t}_2 = \hat{\boldsymbol{k}} = \boldsymbol{e}_3$, the possible choices for $\hat{\boldsymbol{n}}$ are reduced to the options lying in the global coordinate system plane $\boldsymbol{e}_1, \boldsymbol{e}_2$. By rotating $\hat{\boldsymbol{n}}$ several ellipsoidal cross-sections are possible to obtain, allowing a direct 2D and 3D comparison and analysis of the ultrasonic attenuation dimensionality.

2.2 Semi-analytical approach to estimate the Rayleigh ultrasonic waves attenuation

Considering a 3D homogeneous semi-infinite medium defined by x_1, x_2 bounded by a plane perpendicular to x_2, the classical Rayleigh equation (8) can be obtained [13].

$$(2 - \frac{c_R^2}{c_T^2})^2 = 4\sqrt{(1 - \frac{c_R^2}{c_L^2})}\sqrt{(1 - \frac{c_R^2}{c_T^2})} \tag{8}$$

where c_L, c_T, c_R are the longitudinal, transversal and Rayleigh wave velocities. Equation (8) can be rationalized and introducing the dispersion relation $c = \omega/k$, the equation (9) can be obtained.

$$\left(\frac{k_L}{k_R}\right)^6 - 8\left(\frac{k_T}{k_R}\right)^4 + \left(24 - 16\left(\frac{k_L}{k_T}\right)^2\right)\left(\frac{k_L}{k_R}\right)^2 - 16\left(1 - \left(\frac{k_L}{k_T}\right)^2\right) = 0 \tag{9}$$

Equation (9) can be used as a semi-analytical approximation to obtain the complex k_R by knowing the complex k_L and k_T as proposed by [10] with the assumption that the ratio between the imaginary part and the real part of the complex wavenumber is much lower than one that is, $\alpha_i/k_i \ll 1$. The

complex-valued wavenumbers can be obtained by any method such as the one proposed here. It is still an approximation since the relation (9) is obtained by assuming an isotropic homogeneous medium and real-valued wavenumbers k_i, which is not the case for polycrystalline materials.

3 Numerically calculated attenuation from FE simulations

The numerical simulations are carried out using an in-house code with a space-discontinuous Galerkin (sdG) method and an explicit Runge-Kutta scheme in time. Discontinuous Galerkin (DG) methods were originally of interest when dealing with fluid mechanics since in some problems it is necessary to predict actual physical discontinuities [14]. More recently DG methods have been applied to elastodynamic problems with material discontinuities [15]. The DG method used as a solver is a velocity-stress formulation using spatially element-wise discontinuous finite element basis functions.

3.1 Space-discontinuous Galerkin framework

Considering the wave propagation problem in Ω and in the time interval $[0,T]$. Within the framework of the velocity-stress formulation, the governing equations of the elastic wave problem are put into the first-order hyperbolic form, with primary unknowns the velocity and the stress fields $(\boldsymbol{v},\boldsymbol{\sigma})$ [15].

$$\partial_t \boldsymbol{U} + \boldsymbol{A}^{\partial_x}(\boldsymbol{U}) = \boldsymbol{0}, \quad \boldsymbol{A}^{\partial_x}\begin{pmatrix}\boldsymbol{v}\\ \boldsymbol{\sigma}\end{pmatrix} = \begin{pmatrix}-\rho^{-1}\boldsymbol{Div}_x\boldsymbol{\sigma}\\ -\boldsymbol{C}:\varepsilon(\boldsymbol{v})\end{pmatrix} \tag{10}$$

The idea is to approximate the solution with $\boldsymbol{U}_h = (\boldsymbol{v}_h \quad \boldsymbol{\sigma}_h)^T$ that are discontinuous between elements on a finite element mesh. Considering a finite element mesh of the discretized domain Ω, with E being any element and E' any of the neighboring elements of E, the space dG variational formulation for E can be put as $\forall \boldsymbol{W}_h(\boldsymbol{x}) = (\boldsymbol{w}_h(\boldsymbol{x}) \quad \boldsymbol{\tau}_h(\boldsymbol{x}))^T$

$$(\boldsymbol{W}_h, \partial_t \boldsymbol{U}_h)_E + \left(\boldsymbol{W}_h, \boldsymbol{A}^{\partial_x}(\boldsymbol{U}_h)\right)_E + \left(\boldsymbol{W}_h, \hat{\boldsymbol{F}}_n(\boldsymbol{U}_h,\boldsymbol{U}_h') - \boldsymbol{F}_n(\boldsymbol{U}_h)\right)_{\partial E} = 0 \tag{11}$$

where $(\cdot,\cdot)_E$ denotes the integration over the element E of the inner product between two vector or tensor fields. $\hat{\boldsymbol{F}}_n(\boldsymbol{U}_h,\boldsymbol{U}_h')$ denotes the numerical flux that replaces the discontinuous flux $\boldsymbol{F}_n(\boldsymbol{U}_h)$ on the element boundary ∂E.

The sdG method is conditionally stable and therefore, the stability is subjected to the *Courant-Friedrichs-Lewy* condition (CFL). Due to the two-field formulation, the number of degrees of freedom considered is higher than a classical FE method and in consequence, it can be more memory-consuming. However, due to the discontinuity, the resulting mass matrices are composed of diagonal element matrices and together with the explicit time discretization, the parallelization strategies are straightforward.

3.2 Numerical setting and evaluation of the attenuation coefficient

The 3D and 2D microstructure samples are generated using the numerical tool neper [16] by tessellation of the specified number of grains with average grain size distribution. To have elongated grains, a combination of domain scaling and rotation is done, with a final result similar to those shown in Figure 2. The grains are discretized by rasterization of the tessellation as structured FE meshes are used.

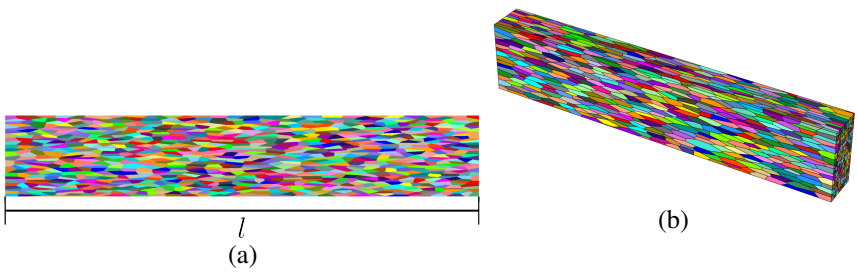

Figure 2: Illustration of (a) 2D and (b) 3D neper generated microstructures with elongated grains.

Simulations are carried out using a Ricker signal applied to the left edge of the sample along with free boundary conditions on the right edge, and symmetric boundary conditions (SBCs) to the remaining edges. The finite-element sizes are chosen such that $h \leq \lambda/10, h \leq \min(a_i)/5$. The time discretization is calculated according to the CFL condition due to the schema used as $\Delta t = CFL * h/c_{max}$, with $CFL = 0.2$ for the specifically used sdG method.

The frequency-dependent amplitude attenuation is calculated using the Fourier Transform of the incident and reflected velocity signals. The incident signal $\hat{v}_y^i(\boldsymbol{p}_j, f)$ is recorded at the probes $\boldsymbol{p}_j$ at the left edge, and the reflected signal $\hat{v}_y^r(\boldsymbol{x}_j, f)$[1] is recorded at the probes $\boldsymbol{x}_j$ at the right edge. Finally, the equation (12) is used to estimate the attenuation:

$$\alpha(f) = -\frac{10}{l} \ln \left(\frac{\sum_{j=1}^{M} \left| \hat{v}_y^r(\boldsymbol{x}_j, f) \right|^2}{\sum_{j=1}^{M} \left| \hat{v}_y^i(\boldsymbol{p}_j, f) \right|^2} \right)^{1/2} \tag{12}$$

where M is the number of recording nodes at each edge and l is the distance traveled by the propagating wave (Figure 2a). To achieve statistical convergence of the evaluated attenuation, several simulations with the same grain configuration but re-randomized Euler angles are carried out. The final attenuation is calculated as an ensemble average of the velocity signals of all the simulations.

4 Results

4.1 Comparison between 3D and 2D theoretical attenuation similarities and differences

We start by comparing the 3D and 2D theoretically estimated ultrasonic attenuation in a titanium-based superalloy for which the material constants are presented in Table 1. The main idea is to analyze the influence of the grain's orientation and the dimensionality in the attenuation. For this purpose, we consider a grain with average radii $a_1 = 0.1\ mm, a_2 = 2a_1, a_3 = 5a_1$. Additionally, we consider three different grain rotations (a), (b) and (c) as presented in Table 2. Moreover, we consider three choices (I, II, III as shown in Table 2) of the unit normal vector $\hat{\boldsymbol{n}}$, representing three different 2D ellipses for each 3D case.

Table 1: Elastic constants and material properties of the titanium-based superalloy and the reference medium.

	$C_{1111}\ (GPa)$	$C_{1122}\ (GPa)$	$C_{1212}\ (GPa)$	ε_L	ε_T	$\rho\ (kg/m^3)$
Titanium	134.0	110.0	36.0	2.74×10^{-2}	1.19×10^{-1}	4428
Reference medium (Voigt average)	153.0	100.0	26.5	0	0	4428

Figure 3 presents the 3D and 2D obtained theoretical results. The obtained attenuation in 3D is comparable to that of previous works [4], [5] and [6]. In the Rayleigh scattering region, the 3D normalized attenuation depends on the grain average volume and has a power behavior of $\alpha_L^{3D} d \propto (fd)^4$, where d is the grain average diameter. In contrast, the 2D normalized attenuation shows a clear cross-section dependency $\alpha_L^{2D} d \propto (fd)^3$ which can be seen explicitly. Looking at each 2D normalized curve one can see that the curve with higher values of attenuation belongs to the planes with a higher cross-section area (I)>(III)>(II) for all three rotations (a), (b) and (c).

At the stochastic scattering region, the normalized attenuation in 3D and 2D are dependent on $d_{||} = 2a_{||}$ the grain size parallel to the wave propagation direction $\hat{\boldsymbol{k}}$. For a larger value of $a_{||}$ ((a)>(b)>(c) see Table 2 and Figures 3a, 3b, 3c), higher values of attenuation are reached. For each case (a), (b) and (c), for each 2D normalized curve, despite the chosen plane (I), (II) or (III), the grain size parallel to $\hat{\boldsymbol{k}}$ remains equal; therefore the convergence to the same attenuation values from the Rayleigh to the stochastic region.

In the Rayleigh-to-stochastic transition region, the 3D attenuation takes higher values than the 2D attenuation in each case, the same behavior as in the case of the equiaxed grains described by Bai *et al.* [12]. In the 2D model, it is also interesting to notice that the cases (a.I) and (c.I) have the same cross-section area due to the axes alignment chosen and therefore both curves (a.I) and (c.I) take the same attenuation values in the lower frequency region (Figure 3a and Figure 3c). Nevertheless, it can be appreciated that at the stochastic scattering region, curve (a.I) takes considerably higher attenuation values than curve (c.I). This demonstrates the cross-section dependency at the Rayleigh scattering region, independent of the grain rotation. At the same time, it demonstrates the ultrasonic attenuation dependency on the grain rotation in the stochastic scattering region.

[1] Due to the superposition of the propagating and reflected wave, the signal $\hat{v}_y^r(\boldsymbol{x}_j, f)$ should be divided by two

Table 2: Ellipse cross-section area (mm^2) and grain radius $a_{||}$ (mm) resulting from each selected normal plane for the three considered grain orientations.

	(I) $\hat{\boldsymbol{n}} = \boldsymbol{e}_1$	(II) $\hat{\boldsymbol{n}} = \boldsymbol{e}_2$	(III) $\hat{\boldsymbol{n}} = \boldsymbol{e}_1 + \boldsymbol{e}_2$	$a_{||}$
(a) $\boldsymbol{g}_1 = \boldsymbol{e}_1, \boldsymbol{g}_2 = \boldsymbol{e}_2, \boldsymbol{g}_3 = \boldsymbol{e}_3$	$\pi/10$	$\pi/20$	$\pi/15.81$	0.5
(b) $\boldsymbol{g}_1 = \boldsymbol{e}_3, \boldsymbol{g}_2 = \boldsymbol{e}_1, \boldsymbol{g}_3 = \boldsymbol{e}_2$	$\pi/20$	$\pi/50$	$\pi/38.08$	0.1
(c) $\boldsymbol{g}_1 = \boldsymbol{e}_1, (\boldsymbol{g}_2, \boldsymbol{e}_2) = 1/\sqrt{2}, (\boldsymbol{g}_3, \boldsymbol{e}_3) = 1/\sqrt{2}$	$\pi/10$	$\pi/38.08$	$\pi/27.84$	0.35

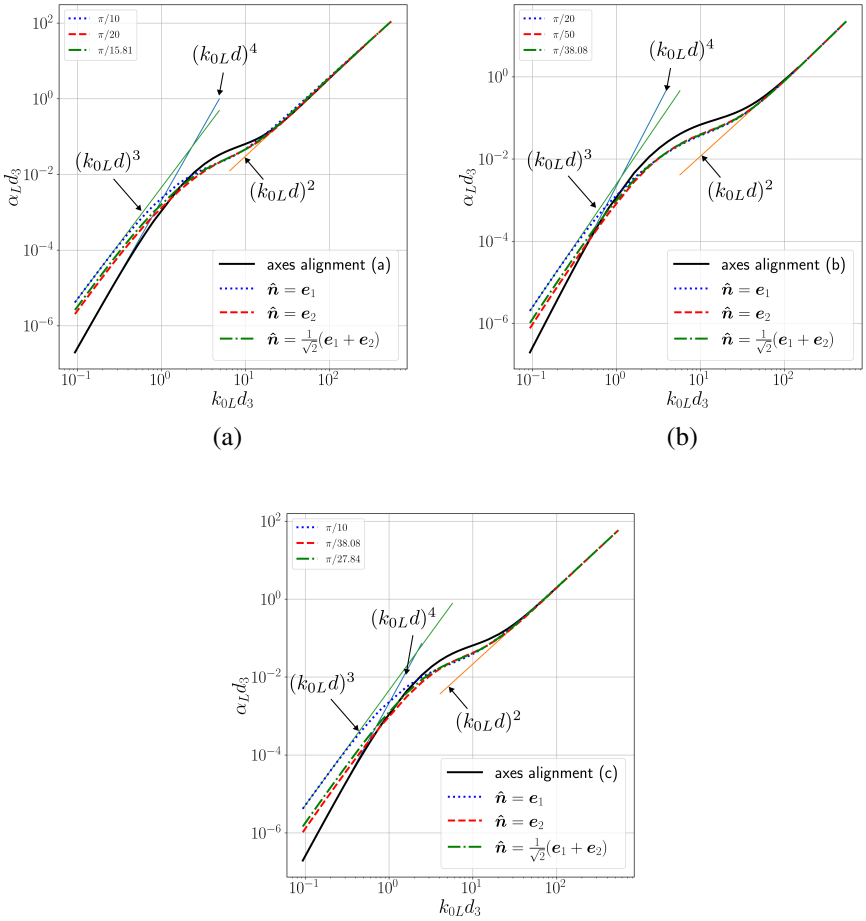

Figure 3: Normalized 3D and 2D attenuation curves with $d_3 = 2a_3$ for a grain with three rotations corresponding to those presented in Table 2 (a), (b) and (c) respectively.

4.2 Comparison between analytically and numerically estimated attenuation

Here we compare the theoretical model for the attenuation with the attenuation numerically evaluated from simulations. In 3D the theoretical and numerical simulations were performed for a grain with $a_3 = 5a_2 = 5a_1$ with $\hat{\boldsymbol{k}} = \boldsymbol{e}_3$. As can be seen in Figure 4a, both normalized attenuation curves are in good agreement in the upper part of the Rayleigh scattering region and the first part of the transition zone. The highest relative difference is $|\alpha_L^{TH} - \alpha_L^{NUM}|/\alpha_L^{NUM} = 34\%$ at the lower frequency values of the numerical curve. In 2D we considered a grain with $a_2 = 5a_1$, with $\hat{\boldsymbol{k}} = \boldsymbol{t}_2$. In the 2D results, we can also see a good agreement (Figure 4b) in the upper part of the Rayleigh scattering region and the upper part of the transition zone. Around $k_{0L}d_2 \approx 3.5$ we find the highest relative difference of 44%. For both 3D and 2D, six simulations were carried out to have a better convergence of the obtained values. The differences can be partially explained by the effect of SBCs which mirror boundary grains and can cause stronger scattering along with the TPC function which ignores this effect [7]. In general, numerical results are a better approach, since the multiple wave scattering is fully considered in contrast with the theoretical model here proposed. In these results, since the simulations were performed in a material with a low level of anisotropy, the numerical and theoretical results are not far from each other. This helps to validate the theoretical model under the initially stated assumptions and limitations.

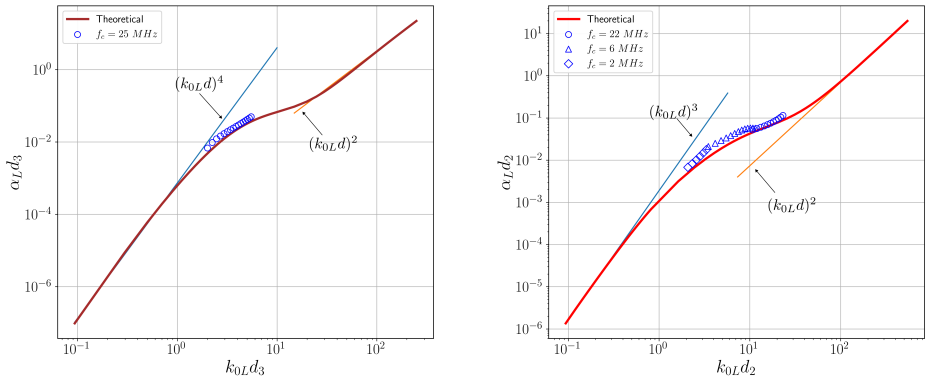

(a) (b)

Figure 4: Numerical and theoretical normalized attenuation curves comparison for (a) 3D grain with $a_3 = 5a_2 = 5_a1$ and (b) 2D grain with $a_2 = 5a_1$.

4.3 Semi-analytical results for the Rayleigh surface wave attenuation

To compare the ultrasonic attenuation of longitudinal (L), transversal (T) and Rayleigh (R) waves, the proposed methodology by Ryzy *et al.* [10] is used here as a first approach. In contrast with the model considered by Ryzy *et al.* [10], the simulation here is done for an elongated grain aligned $\boldsymbol{g}_3 = \boldsymbol{e}_3$ with $a_2 = 2a_1, a_3 = 5a_1$ and a 2D plane defined by the normal $\hat{\boldsymbol{n}} = \boldsymbol{e}_1$ which results in a 2D grain with $a_2 = 5a_1$. The (R) attenuation curve, as can be seen in Figure 5a in 3D and in Figure 5b in 2D, follows the attenuation curve of the transverse (T) wave. This is coherent with Ryzy's [10] result which partially predicts the experimental measures in the stochastic scattering region. However, there is an overestimation of the power law obtained. For two experimental measures [10] obtained a relation $\propto f^{1.61}$ and $\propto f^{1.65}$. In contrast, the semi-analytical approach predicts the power law $\alpha_R \propto f^2$ which is the same power law for the (T) curve. In the Rayleigh scattering region, the (R) curve has a power law $\alpha_R \propto f^4$ in 3D (Figure 5a) which is the same power law obtained by Kaganova *et al.* [9] for equiaxed grains.

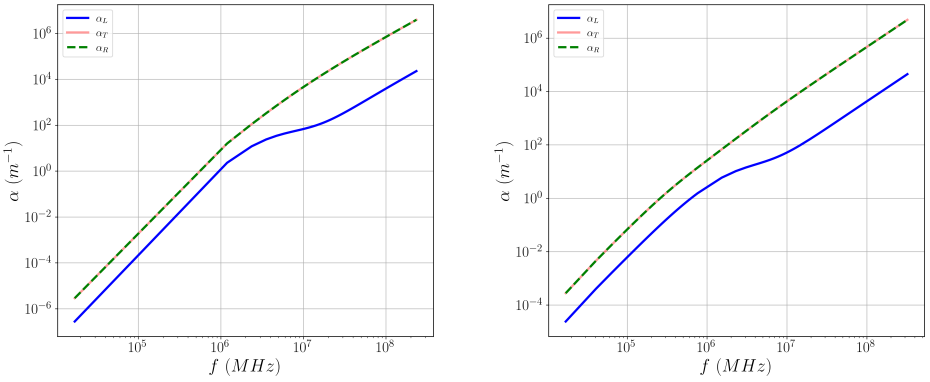

(a) (b)

Figure 5: Normalized attenuation curves for L, T and R waves for (a) 3D elongated grain aligned $\boldsymbol{g}_3 = \boldsymbol{e}_3$ with $a_2 = 2a_1, a_3 = 5a_1$ and $\hat{\boldsymbol{k}} = \boldsymbol{e}_3$ and (b) 2D elongated grain obtained with $a_2 = 5a_1$ and $\hat{\boldsymbol{k}} = \boldsymbol{t}_2$.

5 Conclusions and perspectives

A 3D and 2D model for the ultrasonic attenuation in microstructures with elongated grains was obtained. Numerical simulations were carried out using an sdG method. Both theoretically and numerically estimated attenuations were found to be in good agreement, which shows the validity of the considered assumptions in the theoretical models. Furthermore, the attenuation in the 2D case was found to be proportional to the cross-section (power law of f^3, in contrast to the 3D case f^4) in the Rayleigh scattering region. In the stochastic scattering region, both in 3D and 2D, the attenuation was found to be dependent on the grain size parallel to the wave propagation direction $\hat{\boldsymbol{k}}$ (power law of f^2). As a first result, the

Rayleigh wave attenuation in elongated grains was found to follow a behavior similar to the transverse attenuation, however is already stated that the power law is overestimated in the higher frequencies. The sdG-Runge Kutta is a versatile solver for which MPI parallelization strategies are straightforward to implement. It is, however, necessary to have a balanced memory transfer between processes due to the large number of degrees of freedom and therefore the memory that is occupied by the FE matrices. Optimization during the mesh distribution stage, looking for an even partition of memory required in each process, is to be done. It is also intended in future work to carry out numerical simulations of Rayleigh waves to have a more representative analysis of their scattering mechanisms.

References

[1] Fred E Stanke and Gordon S Kino. A unified theory for elastic wave propagation in polycrystalline materials. *The Journal of the Acoustical Society of America*, 75(3):665–681, 1984.

[2] Frank C Karal Jr and Joseph B Keller. Elastic, electromagnetic, and other waves in a random medium. *Journal of Mathematical Physics*, 5(4):537–547, 1964.

[3] Richard L Weaver. Diffusivity of ultrasound in polycrystals. *Journal of the Mechanics and Physics of Solids*, 38(1):55–86, 1990.

[4] S. Ahmed. Ultrasonic Attenuation as Influenced by Elongated Grains. In *AIP Conference Proceedings*, volume 657, pages 109–116, Bellingham, Washington (USA), 2003. AIP. ISSN: 0094243X.

[5] L. Yang, O.I. Lobkis, and S.I. Rokhlin. Shape effect of elongated grains on ultrasonic attenuation in polycrystalline materials. *Ultrasonics*, 51(6):697–708, August 2011.

[6] Marie Calvet and Ludovic Margerin. Impact of grain shape on seismic attenuation and phase velocity in cubic polycrystalline materials. *Wave Motion*, 65:29–43, September 2016.

[7] M. Huang, G. Sha, P. Huthwaite, S. I. Rokhlin, and M. J. S. Lowe. Maximizing the accuracy of finite element simulation of elastic wave propagation in polycrystals. *The Journal of the Acoustical Society of America*, 148(4):1890–1910, October 2020.

[8] M. Huang, G. Sha, P. Huthwaite, S. I. Rokhlin, and M. J. S. Lowe. Longitudinal wave attenuation in polycrystals with elongated grains: 3D numerical and analytical modeling. *The Journal of the Acoustical Society of America*, 149(4):2377–2394, April 2021.

[9] I M Kaganova and A A Maradudin. Surface acoustic waves on a polycrystalline substrate. *Physica Scripta*, T44:104–112, January 1992.

[10] Martin Ryzy, Tomáš Grabec, Johannes A Österreicher, Mike Hettich, and István A Veres. Measurement of coherent surface acoustic wave attenuation in polycrystalline aluminum. *AIP Advances*, 8(12):125019, 2018.

[11] Xue Bai. *Modélisation par éléments finis de la propagation des ondes ultrasonores dans des matériaux polycristallins*. PhD thesis, Université Paris-Saclay (ComUE), 2017.

[12] X Bai, B Tie, J-H Schmitt, and D Aubry. Comparison of ultrasonic attenuation within two-and three-dimensional polycrystalline media. *Ultrasonics*, 100:105980, 2020.

[13] Karl F Graff. *Wave motion in elastic solids*. Courier Corporation, 2012.

[14] Bernardo Cockburn, George E Karniadakis, and Chi-Wang Shu. The development of discontinuous galerkin methods. In *Discontinuous Galerkin methods: theory, computation and applications*, pages 3–50. Springer, 2000.

[15] Bing Tie. Some comparisons and analyses of time or space discontinuous Galerkin methods applied to elastic wave propagation in anisotropic and heterogeneous media. *Advanced Modeling and Simulation in Engineering Sciences*, 6(1):3, December 2019.

[16] R. Quey, P.R. Dawson, and F. Barbe. Large-scale 3D random polycrystals for the finite element method: Generation, meshing and remeshing. *Computer Methods in Applied Mechanics and Engineering*, 200(17-20):1729–1745, April 2011.